Surfactant-free synthesis uniform $Ti_{1-x}Sn_xO_2$ nanocrystal colloids and their photocatalytic performance

Yin Zhao*, Jia Liu, Liyi Shi*, Shuai Yuan, Jianhui Fang, Zhuyi Wang, Meihong Zhang

Research Center of Nanoscience and Nanotechnology, Shanghai University, 99 Shangda Road, Shanghai 200444, PR China

ARTICLE INFO

ABSTRACT

The preparation of $Ti_{1-x}Sn_xO_2$ nanocrystal colloids from peroxo-metal precursor by hydrothermal method was reported in this work. The obtained materials were investigated by means of XRD, Raman, TEM, XPS, ICP-AES, N_2 adsorption–desorption measurements (BET), PL and UV–vis spectroscopies technology. Photocatalytic degradation of phenol was studied under UV illumination. The results indicated that $Ti_{1-x}Sn_xO_2$ nanocrystal colloids were obtained in the nanometer scale (less than 10 nm) and the crystallite size was smaller than pure TiO_2. Anatase phase, mixture phase (anatase and rutile) and rutile phase of Sn-doped TiO_2 samples were formed, when $x < 0.04$, $0.04 < x < 0.06$ and $x \geq 0.06$, respectively. The Sn^{4+} dopants presented substitution Ti^{4+} into the lattice of TiO_2 alongside increasing the surface oxygen vacancies and the surface hydroxyl groups. Regarding photocatalytic activity, Sn-doped TiO_2 samples (TiSn3) were nearly four times higher than undoped samples. This obvious beneficial effect could be attributed to high surface area, optimal crystalline phase and surface state modifications.

1. Introduction

TiO_2 is an attractive semi-conductive material due to its potential application in the wide range of fields such as conventional catalyst support, pigment, photocatalysts, solar cells, photochromic devices and sensors [1–5]. The applications of TiO_2 are strongly dependent on its crystal structure and morphology as well as grain size [6]. Three polymorphs, rutile, anatase, and brookite occur in nature, in which rutile is the thermodynamically stable form, whereas anatase and brookite are metastable [7]. Each of the three crystallographic forms of TiO_2 exhibits different physical properties, such as refractive, chemical reactivity and photochemical activity, making them suitable for different applications [8]. For example, rutile TiO_2 is the most stable phase even in strongly acidic or basic environments and has higher dielectric constant and better photo-absorption property in visible light wavelength range (>400 nm) [9–11]. But anatase TiO_2 is usually considered to be more active than rutile crystalline in the photodegradation of many pollutants in water and air, which can be attributed that anatase possesses a slightly higher Fermi level and a higher degree of surface hydroxylation [12].

Nowadays, many methods such as sol–gel process [13], hydrothermal method [14] solvothermal method [15] and emulsion precipitation [16] have been developed for the synthesis of TiO_2 nanoparticles. However, the TiO_2 nanoparticles synthesized via most of the traditional routes are amorphous. Consequently, additional calcinations are generally required to induce crystallization, which frequently leads to the particle growth and agglomeration [17]. Generally, rutile is prepared by calcination from anatase at high temperatures. Such a thermal annealing may cause hard aggregation by inter-particles sintering or the formation of large particle sizes and decrease the extents of surface hydroxylation, which depress photocatalytic activity [18]. In addition, the crystal stability is size-dependent, and it has been reported that, when the particle diameter is below 14 nm, anatase is the most stable form. Above 35 nm, rutile is preferred [19]. Therefore, obtaining high surface area, small particles size and highly crystalline rutile TiO_2 at lower temperature is still a challenge.

Currently, many efforts have been made to decrease the formation temperature of rutile phase [20–22]. Suresh et al. found that by controlling pH of the precursor, the anatase–rutile phase transformation temperature could be changed, but the range of pH studied was very narrow [23]. Gopal et al. have synthesized rutile TiO_2 at low temperature ($T \leq 100\,°C$) by hydrolysis of a titanium alkoxide in the acidic solution at certain temperature [24]. Other reports showed that rutile can be obtained from titanium solutions, when seeds of oxides with the rutile-type structure are embedded into it. For example Fe, Sn, Th, Cu, Pd and other dopants can assist the phase transformation at lower temperatures due to so-called strong-metal-support-interaction. The transition of doped TiO_2 from anatase to rutile takes place at ca. 400 °C unlike undoped

* Corresponding authors. Tel.: +86 21 66134852; fax: +86 21 66134852.
E-mail addresses: zhaoyin@shu.edu.cn (Y. Zhao), shiliyi@shu.edu.cn (L. Shi).

TiO_2 which shows the anatase to rutile transition at ca. 800 °C [25–28].

Despite much progress in the synthesis of TiO_2 at relatively low temperature, the direct growth of TiO_2 nanocrystalline colloidal (less than 10 nm) with controlled crystalline phase and morphology is still not well exploited. Moreover, the detailed investigation about the physicochemical properties of above TiO_2 architectures is still desired to understand. In our previous studies, we synthesized anatase nanocrystal colloidal from peroxo-titanium acid (PTA) by solvothermal method [29]. This PTA approach gives pure anatase by oxidizing amorphous titanium hydroxide precipitates using hydrogen peroxide, followed by the solvothermal treatment under low temperature and neutral pH condition. The strategy of this work is to explore a facile route for the synthesis of controlled crystalline phase and morphology TiO_2 nanocrystal colloids under low temperature.

Herein, TiO_2 nanocrystal colloids by doping with Sn^{4+} ions were prepared from PTA by hydrothermal method in this research. Controlled Sn/Ti atomic ratios, ranging from nominal 0% to 10% were used in order to prepare $Ti_{1-x}Sn_xO_2$ nanocrystal colloids. The effects of the Sn^{4+} dopant concentration on the essential structural properties of the resultant colloids such as the phase formation, the crystalline phase, the average particle diameters and the distributions were systematically investigated. The liquid-phase photocatalytic degradation of phenol is used as a model reaction to test the photocatalytic activity of the synthesized materials. To the best of our knowledge, the synthesis of $Ti_{1-x}Sn_xO_2$ nanocrystal colloids using hydrothermal method from peroxo-metal complex solution precursors is reported for the first time.

2. Experimental

2.1. Materials

All chemicals were used as received without further purification. Titanium (IV) sulfate ($Ti(SO_4)_2$, CR) and tin (IV) tetrachloride penthydrated ($SnCl_4·5H_2O$, CR) was provided by Shanghai Chemical Reagent Co., China. Aqueous ammonia solution (NH_4OH, 25%, AR) and aqueous hydrogen peroxide solution (H_2O_2, 30%, AR) were purchased from Sinopharm Chemical Reagent Co. Ltd. Deionized water was used for solution preparation.

2.2. Preparation of $Ti_{1-x}Sn_xO_2$ nanocrystal colloids

For the synthesis of $Ti_{1-x}Sn_xO_2$ nanocrystal colloids, ranging from $x = 0$ (TiSn0) to $x = 0.10$ (TiSn10), the appropriate quantities of $Ti(SO_4)_2$ and $SnCl_4·5H_2O$ were diluted with deionized water to be a 125 mL of 0.1 M solution. Under vigorous stirring, 3 M ammonia solution was slowly added, adjusting the pH value to 7.5, which produced a white precipitate in the solution immediately. After that, the resulting suspension was filtered and washed. A purified white precipitate was then obtained. The obtained cake was redispersed in 125 mL water and ultrasonically dispersed. Under continuous magnetic stirring, 5 mL of H_2O_2 (30 wt.%) was added dropwise to the suspension. The mixture was refluxed at 95 °C for 4 h. Finally, the resulting hydrothermal precursor was transferred to an autoclave, and then held at 180 °C for 15 h. After the hydrothermal crystallization, the prepared $Ti_{1-x}Sn_xO_2$ nanocrystal colloids were thus obtained.

2.3. Characterization

The $Ti_{1-x}Sn_xO_2$ powders were prepared through rotatory evaporation of the $Ti_{1-x}Sn_xO_2$ colloids at 45 °C for the following testing. The X-ray diffraction (XRD) patterns of the samples were measured using a Rigaku D/MAX-2000 X-ray diffractometer with Cu Kα radi-

ation (λ = 0.15418 nm). The average particle size was calculated by the Scherrer equation from the width of the most intense reflections: (1 0 1) for anatase and (1 1 0) for rutile. Rutile/anatase weight ratios were also estimated from the XRD data by means of Eq. (1):

$$W_R = \frac{A_R}{0.884A_A + A_R} \tag{1}$$

where W_R is the proportion of rutile, and A_A and A_R are the integrated areas of the (1 0 1) peak of anatase and the (1 1 0) peak of rutile, respectively [17,30]. The Raman spectra were recorded on an in Via + Reflex spectrometer equipped with an optical microscope at room temperature, For excitation, the 514.5 nm line from an Ar^+ ion laser (Spectra Physics) was focused, with an analyzing spot of about 1 µm, on the sample under the microscope. The power of the incident beam on the sample was 1 mW. The time of acquisition was varied according to the intensity of the Raman scattering. Transmission electron microscopy (TEM) images were taken with a JEOL JEM-200 CX microscope electron microscope. X-ray photoelectron spectroscopy (XPS) spectra were recorded by a PHI 5000C ESCA spectrometer using Mg Ka radiation ($h\nu$ = 1253.6 eV). The pressure of the analyzer chamber was maintained at 5×10^{-8} Pa. The shift of the binding energy due to relative surface charging was corrected using the C 1s level at 284.6 eV as an internal standard. The experimental spectra were resolved into Lorentzian–Gaussian components after subtraction of a linear background, using a nonlinear least squares fitting route. The quantitative analysis of the sample was performed using the route software of the XPS instrument with appropriate sensitivity factors. Elemental analysis was carried out by inductively coupled plasma atomic emission spectroscopy (ICP-AES) at Optima 7300DV. The zeta potential of $Ti_{1-x}Sn_xO_2$ nanocrystal colloids was measured on a Zeta sizer 3000HS (Malvern Instruments Ltd., UK). The specific surface areas of the samples were determined through nitrogen adsorption at 77 K on the basis of BET equation (model 3H-2000III, China). Diffuse reflectance spectra (DRS) were obtained for the dry-pressed disk samples using a Scan UV–vis–NIR spectrophotometer (Varian, Cary 500) equipped with an integrating sphere assembly, using $BaSO_4$ as reflectance sample. The photoluminescence (PL) spectra were measured through fluorescence spectrophotometer (Hitachi, F-7000) using 300 nm line of Xe lamp as excitation source at room temperature.

2.4. Photocatalytic degradation of phenol

Phenol is a representative phenolic compound in aqueous solutions and a major industrial pollutant, which causes severe environment problems. The photocatalytic activities of the $Ti_{1-x}Sn_xO_2$ nanocrystal colloids were evaluated by photocatalytic degradation of phenol under UV light illumination. 0.07 g of each catalyst was suspended in 70 mL phenol aqueous solution (10 mg/L) using 120 mL quartz tube and using a magnetic stirrer to better stirring. The black light lamps (GE, F8T5/BLB) were used as an illuminating source symmetrical placed around reactor and the irradiation intensity is 0.55 mW/cm^2. The catalysts were agitated for 30 min in phenol solution in the absence of light to attain the equilibrium adsorption on the catalyst surface. After a given irradiation time, the samples were withdrawn for subsequent analysis with a UV–vis spectrophotometer (UV-2501 PC spectrometer). The efficiency of degradation was calculated from formula (2) as follows:

$$\text{Phenol degradation } (\%) = \frac{(C_0 - C)}{C_0} \times 100\% \tag{2}$$

where C_0 and C are the original phenol concentration after the adsorption/desorption reached equilibrium and residual phenol concentration after reaction.
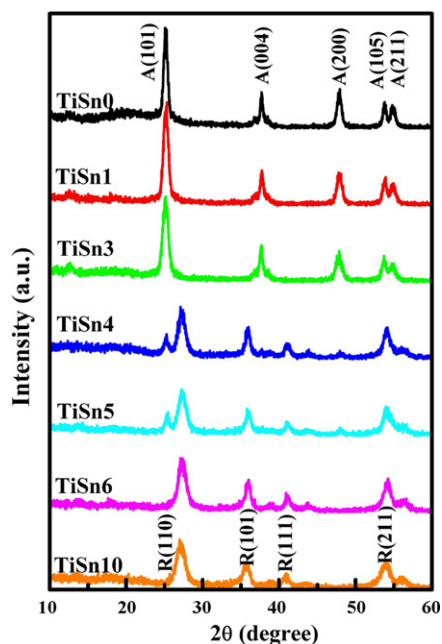
Fig. 1. XRD patterns of $Ti_{1-x}Sn_xO_2$ nanocrystal colloids. A: anatase, R: rutile.

Fig. 2. Raman spectra for $Ti_{1-x}Sn_xO_2$ nanocrystal colloids. A: anatase, R: rutile.

3. Results and discussion

Fig. 1 shows the XRD patterns of $Ti_{1-x}Sn_xO_2$ samples. The pattern of undoped titania sample (TiSn0) is indexed as anatase phase of TiO_2 (JCPDS File No. 21-1272). This is in agreement with previously reported results for pure TiO_2 at the same prepared method [29]. Samples TiSn1 and TiSn3 also exhibit a single anatase phase. However, increasing Sn^{4+} doping content leads to forming rutile structure. A mixture of anatase and rutile (JCPDS File No. 65-0192) crystalline form of TiO_2 with an obvious predominance of the rutile phase is observed in samples TiSn4 and TiSn5. Rutile appears as the only crystalline phase in samples TiSn6 and TiSn10. Briefly, the higher Sn^{4+} doping content leads to the formation of rutile phase in the higher proportion (shown in Table 1). Moreover, all diffraction peaks corresponding to SnO_2 are not present in the pattern of all $Ti_{1-x}Sn_xO_2$ samples [31]. On the basis of this, it can be inferred that either the Sn^{4+} ion has been substituted into the crystal lattice sites of the titania or tin oxide exists as a highly dispersed polymeric form over the titania surface, which could not be detected by XRD.

The significant changes in the phase structure of $Ti_{1-x}Sn_xO_2$ samples can be well explained by the addition of dopant Sn^{4+}. The ionic radius of Sn^{4+} is 0.69 å and it is likely to substitute for Ti^{4+} (with an ionic radius of 0.68 å) in the TiO_2 lattice [32,33]. Further, the crystal structure of SnO_2 is similar to the rutile titania. Both of them belong to the tetragonal crystal symmetry with the space group $P4_2/mnm$ and two molecular units per primitive unit cell ($Z = 2$), also
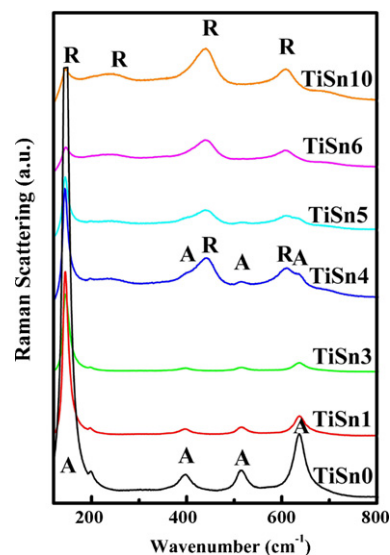
have very similar lattice parameters [34]. Therefore, the addition of Sn^{4+} into TiO_2 assists crystallization in rutile structure, and the formation of rutile has been observed in previously reported tin-doped TiO_2 samples obtained by other procedures such as sol–gel, solovothermal method, reverse microemulsions and combustion [35–38]. In addition, the obtained phase composition and stability depend on the preparation technique or crystallization method, their conditions (e.g. precursor materials and their concentration, composition, pH, treatment temperature), the amount of dopant, etc. In our prepared procedure, the minimum Sn^{4+} content leads to rutile phase formation is 4 mol.%. The average crystalline sizes of all synthesized samples were calculated using Scherrer formula and collected in Table 1. The anatase crystalline size gradually decreased from 16.1 to 9.8 nm with the increasing Sn^{4+} content, from TiSn0 to TiSn3. After that, an obvious increase to 15.5 and 18.8 nm can be observed (samples TiSn4 and TiSn5). In the case of the rutile phase, the crystalline size slightly decreases from 8 to 7 nm with enhancing the Sn^{4+} doping levels from TiSn4 to TiSn10. Generally, Sn^{4+} doping TiO_2 can inhibit the growth of crystal grains due to the presence of Ti–O–Sn [39]. However, an interesting trend for anatase crystalline size, that is, a first decrease at low dopant level and an obvious increase at high dopant level is observed. It is ascribed to the fact that the dopant Sn^{4+} concentrated in rutile and has a lower effect on anatase when both phases coexist [36]. This assumption can be confirmed from the experiment results that rutile crystals are smaller than the anatase crystals in the case of coexistence of anatase and rutile phase samples. According to the report by Overstone and Yanagisawa [40], a critical particle size is required for the anatase to rutile transformation. However, a differ-

Table 1
Characteristics of $Ti_{1-x}Sn_xO_2$ nanocrystal colloids.

Sample	$Ti_{1-x}Sn_xO_2$		XRD measurements		S_{BET} (m²/g)	ξ (mV)	Band gap (E_g)
	Calculated x	Obtained x(ICP)	Phase detected	Crystallite size (nm)			
TiSn0	0	0	Anatase	16.1	83.2	−52.9	3.25
TiSn1	0.01	0.0091	Anatase	11.6	121.2	−53.6	3.30
TiSn3	0.03	0.031	Anatase	9.8	134.8	−58.0	3.30
TiSn4	0.04	0.041	Anatase (12.5%)	15.5	119.9	−63.6	3.10
			Rutile	7.8			
TiSn5	0.05	0.050	Anatase (9.9%)	18.8	130.6	−63.7	3.15
			Rutile	8.1			
TiSn6	0.06	0.062	Rutile	7.3	138.4	−55.8	3.10
TiSn10	0.10	0.10	Rutile	7	152.7	−57.6	3.10
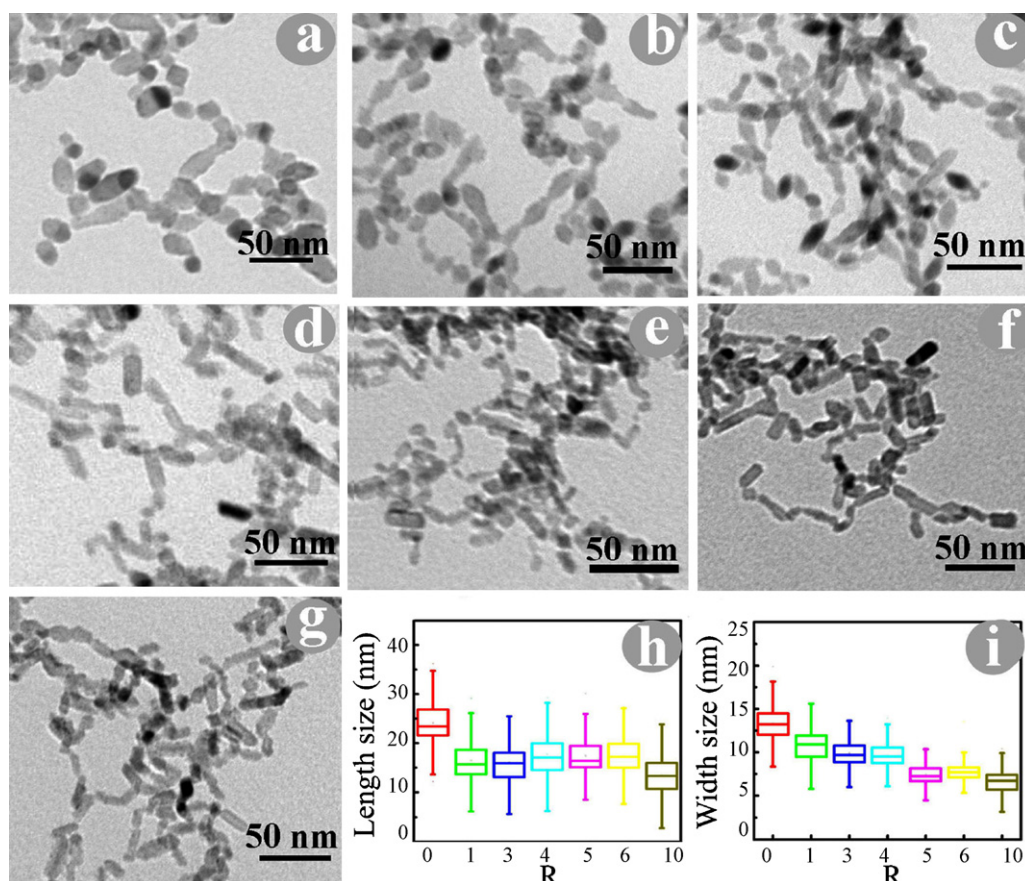
Fig. 3. TEM images for $Ti_{1-x}Sn_xO_2$ nanocrystal colloids: (a) TiSn0, (b) TiSn1, (c) TiSn3, (d) TiSn4, (e) TiSn5, (f) TiSn6, (g) TiSn10, the statistical evaluation of long axis size (h) and the short axis size (i) estimated by the measurement of at least 100 particles in the TEM images. R represents the samples from TiSn0 to TiSn10.

ent trend is obtained in our work, which indicates rutile formation occurs through a different mechanism, favored by tin incorporation.

The phase evolution of the $Ti_{1-x}Sn_xO_2$ nanocrystal colloids obtained in this work was also investigated by Raman spectroscopy. In Fig. 2, four well-established bands at 146, 398, 514, and 638 cm^{-1}, which are characteristic of anatase phase [41], observed in the samples TiSn0 TiSn1 and TiSn3. Upon further increasing the level of Sn^{4+} doping (samples TiSn4 and TISn5), three strong peaks at 143, 443, 609 cm^{-1}, which are very similar to those of rutile TiO_2 [42], were observed. Additional three weak Raman peaks assigned to anatase phase of TiO_2: 398, 517 and 636 cm^{-1} are also recognized in samples TiSn4 and TISn5, which indicate two-phase coexistence with predominance of the rutile phase. When Sn^{4+} content is higher (more than 6 mol.%), only rutile phase peaks at 146, 438 and 609 cm^{-1} were observed in samples TiSn6 and TiSn10. In accordance with the XRD results, the Raman results also prove that the crystalline structure of $Ti_{1-x}Sn_xO_2$ samples varies with Sn^{4+} dop-

ing content. The main Raman bands at 776, 636, 574, and 490 cm^{-1} attributed to SnO_2 crystalline are all undetectable, which indicates that tin does not exist as a separate crystalline oxide phase [43]. There is also a significant decrease in the intensity of the Raman peaks with the increasing Sn^{4+} doping concentration. It is well known that the vector rule breaks down with a break in symmetry [44]. The lowering of the intensity of the Raman peaks as a function of Sn^{4+} content indicates a breaking of the total symmetry of the TiO_2 molecular structure. Therefore, it can be inferred that Sn^{4+} is doped in the titania lattice which corroborates the XRD results.

The particle morphologies and size statistical graph of the undoped TiO_2 and as-prepared $Ti_{1-x}Sn_xO_2$ samples were characterized by TEM observations (Fig. 3). In the displayed TEM images, all the samples are uniform and well dispersed. The undoped TiO_2 consists of "spindle like" anatase particles, which have lengths of about 21 nm and widths of about 13 nm (Fig. 3a, h and i). In low dopant level, $Ti_{1-x}Sn_xO_2$ samples also display the similar shape, but the particle size is smaller than undoped sample, whose length

Table 2
Surface analysis by XPS spectra for $Ti_{1-x}Sn_xO_2$ nanocrystal colloids.

Sample	Binding energy (eV)				$Ti_{1-x}Sn_xO_2$, x obtained from XPS	O_L%	O_H%	SOV content/%[a]
	Ti $2p_{3/2}$	Sn $3d_{5/2}$	O_L 1s(Ti–O)	O_H 1s(O–H)				
TiSn0	458.8	–	529.82	531.33	0	60.1	39.9	21.0
TiSn3	458.2	486.0	529.63	531.28	0.06	56.1	42.6	21.1
TiSn5	458.4	486.0	529.50	531.02	0.07	57.4	42.6	26.4
TiSn10	458.3	486.4	529.58	531.16	0.14	55.6	44.4	24.8

[a] SOV represent the surface oxygen vacancies (SOV) of $Ti_{1-x}Sn_xO_2$ nanocrystal colloids. The SOV can be estimated using the equation [45]: SOV $= (2 - R)/2 \times 100\%$, where $R = O_L$ mol.%/(Ti mol.% + Sn mol.%).
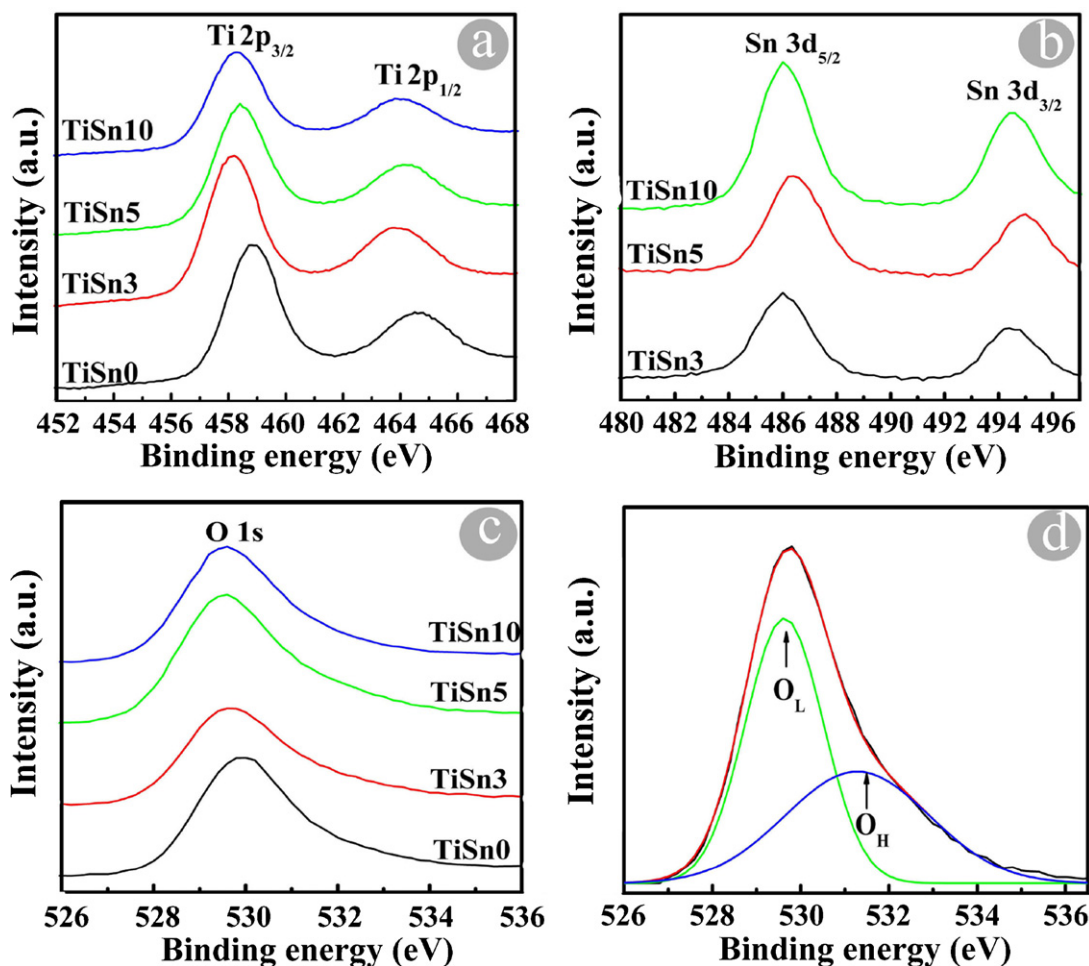
Fig. 4. (a) Ti 2p, (b) Sn 3d, (c) O 1s XPS core level spectra of $Ti_{1-x}Sn_xO_2$ nanocrystal colloid samples and (d) O 1s fitting results for sample TiSn3.

decreases to about 16 nm and width decreases to about 10 nm (Fig. 3b, c, h and i). However, in high dopant level, when rutile phase appears, the shapes of $Ti_{1-x}Sn_xO_2$ samples transform to "rod-like" structure (Fig. 3d–g). Moreover, the particles size still decreases with the increasing of the Sn^{4+} doping.

BET surface areas of $Ti_{1-x}Sn_xO_2$ nanocrystal colloid samples are shown in Table 1. Reduction in the particle size was caused by doping Sn^{4+} ion led to larger surface area. From Table 1, it could be seen that the surface area obviously increased; even when a small amount of Sn^{4+} (samples TiSn1 and TiSn3) was introduced into TiO_2. There was a significant increase of specific surface area from 83.2 to 134.8 $m^2\,g^{-1}$. However, the surface area decreases to 119.9 $m^2\,g^{-1}$ for the sample TiSn4, it can be inferred that the large anatase crystallites size in two-phase coexistence samples leads to the slight decrease of surface area. When the Sn^{4+} content was further increased, rutile phase became predominant, the surface area gradually increased. The maximum surface area was observed for TiSn10 samples with a value of 152.7 $m^2\,g^{-1}$. It is confirmed from XRD and TEM analysis that particle sizes of prepared samples is strongly dependent on Sn^{4+} content. With the increase of Sn^{4+} content, particles size decreased, resulting in the increase of surface area.

The surface composition and chemical states of $Ti_{1-x}Sn_xO_2$ nanocrystal colloid samples ($x = 0, 3, 5$ and 10) were tested by XPS method. Fig. 4 shows the XPS spectra of Ti 2p (a), Sn 3d (b) and O 1s (c and d). From the Ti 2p XPS spectra of the TiSn0, TiSn3, TiSn5 and TiSn10 samples depicted in Fig. 4a, the spin–orbit components ($2p_{3/2}$ and $2p_{1/2}$) of the peak were well deconvoluted by two curves

(at approximately 458.8 and 464.5 eV, respectively), indicating that the Ti element mainly existed as the chemical state of Ti^{4+} [46]. Interestingly, the binding energies of Ti $2p_{3/2}$ and Ti $2p_{1/2}$ shifted to lower values after the addition of dopant Sn^{4+} compared to pure TiO_2 (Fig. 4a and Table 2). This shift can prove the existence of Ti with lower valence. The formation of Ti with lower valence can be attributed to the existence of oxygen vacancies in the nanoparticles after doping Sn. XPS spectra of Sn 3d region are given in Fig. 4b. Owing to spin–orbit coupling effect, two peaks corresponding to Sn $3d_{5/2}$ and Sn $3d_{3/2}$ are observed. The peak position corresponding to Sn $3d_{5/2}$ (Table 2) is located between those of Sn $3d_{5/2}$ in SnO_2 (486.5 eV) and Sn $3d_{5/2}$ in metallic Sn (485.0 eV), which ascribed to incorporated Sn^{4+} in the lattice of TiO_2 [47]. The XPS spectra of O 1s core level of TiSn0, TiSn3, TiSn5 and TiSn10 samples are asymmetric (Fig. 4c), indicating that there are at least two kinds of chemical states. After curve fitting, besides the peak corresponding to the lattice oxygen of TiO_2 (O_L), the other peak at higher binding energy can be identified (Fig. 4d). This peak should be attributed to the surface species such as Ti–OH and Ti–O–O resulting from the chemisorbed water (O_H) [48]. The fitting results listed in Table 2 give the corresponding XPS data, atomic number ratio and relative content of surface oxygen vacancies. As seen from Table 2, the amount of surface hydroxyl oxygen and oxygen vacancies is enhanced by doping Sn^{4+}. The oxygen vacancies are a very active group, which can easily combine with other atoms or groups to become stable, and it accounts for an increase in the amount of the surface hydroxyl oxygen. An increase in the surface hydroxyl is favorable to photocatalytic reactions [49].
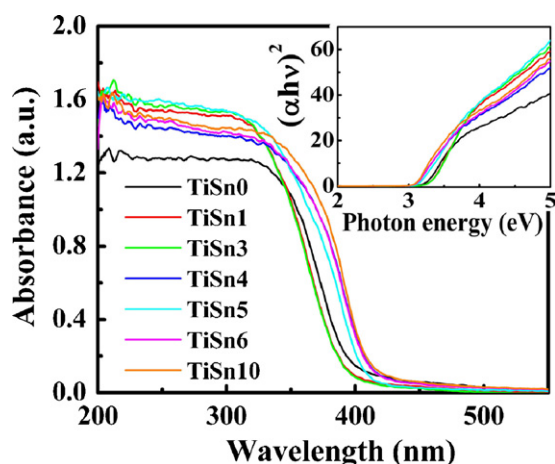
Fig. 5. UV–vis diffuse reflectance spectra of $Ti_{1-x}Sn_xO_2$ nanocrystal colloids.

Fig. 5 shows the UV–vis diffuse reflectance spectra of $Ti_{1-x}Sn_xO_2$ samples. The optical band gap energy can be estimated using the following equation for a semiconductor:

$$\alpha = \frac{K(h\nu - E_g)^{n/2}}{h\nu} \tag{3}$$

where α is the absorption coefficient, K is a constant, E_g is the band gap, and n is equal to 1 for a direct transition. The band gap can be estimated from a plot of $(\alpha h\nu)^2$ versus photon energy ($h\nu$). The intercept of the tangent to the plot will give a good approximation of the band gap energy for this direct band gap material (shown in the inset of Fig. 5) [50]. The band gap energies of $Ti_{1-x}Sn_xO_2$ samples are calculated and listed in Table 1. From the Fig. 5, all of the samples display an absorption edge corresponding to the UV region. Compared with the undoped TiO_2 sample, all the Sn^{4+}-doped TiO_2 samples showed much stronger light absorption property in the UV region. In the case of low dopant level, curves TiSn1 and TiSn3 of Fig. 5 exhibit a blue shift as compared to the undoped titania (curves TiSn0), and the band gap energy increases from 3.25 to 3.30 eV. This blue shift and enhance in band gap suggest electronic modifications of anatase due to the dopant cations [34]. However, the absorption edge gradually shifted towards red region as increasing the amount of Sn^{4+} doping (curves TiSn4, TiSn5, TiSn6 and TiSn10) and the band gap energy reduces to about 3.1 eV, which can be due to the fact that phase transforms from anatase to rutile lead to the decrease of band gap [51].

The fluorescence emitted by the $Ti_{1-x}Sn_xO_2$ samples was also observed in this study. Fig. 6 shows the broad PL spectra of the samples TiSn0, TiSn3, TiSn5 and TiSn10, excited by a laser with a wavelength of 300 nm. All the samples exhibited a broad peak at about 400 nm, which arose from the luminescence of self-trapped excitons [52]. The PL emission peaks of TiSn5 and TiSn10 are red shifted compared with that of TiSn0 and TiSn3, which is consistent with the evaluated band gap according to the UV–vis spectra (Fig. 5 and Table 1). Some other peaks with central wavelength beyond 400 nm in the PL spectra resulted possibly from the surface states and oxygen vacancies. Serpone et al. reported that the PL bands of anatase nanocrystals at the long wavelength range (442, 455, 465, and 502 nm) were attributed to oxygen vacancies [53]. From the spectral lines it was clearly observed that the PL spectrum of Sn^{4+}-doped TiO_2 samples was of much stronger intensity than that of undoped TiO_2 sample, which may be attributed that the Sn^{4+}-doped TiO_2 nanoparticles with high surface-to-volume ratio should also favor the existence of large quantities of oxygen vacancies [54]. This result is also confirmed from the XPS analysis. The photoluminescence emission spectra have been widely used to investigate
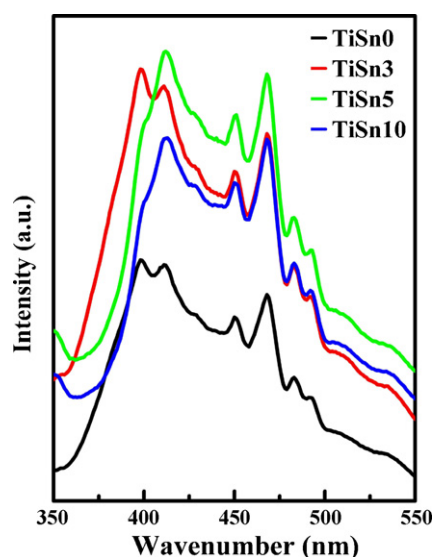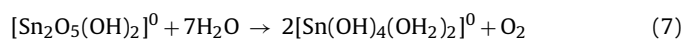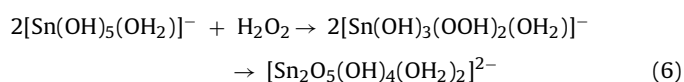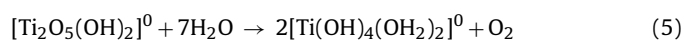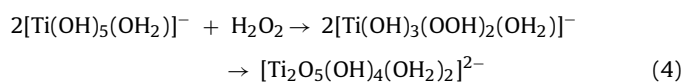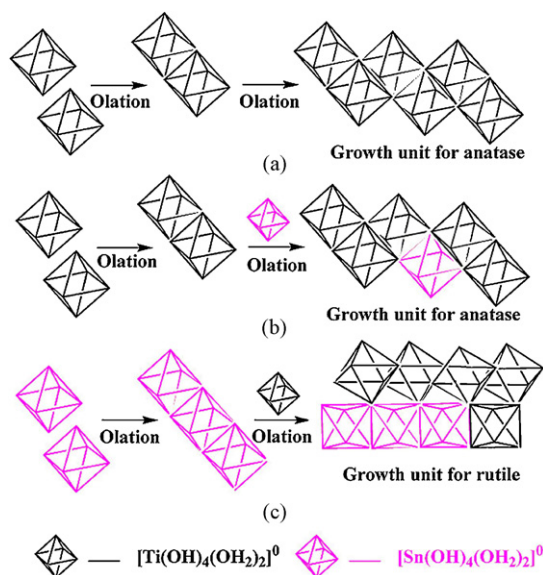

Fig. 6. Photoluminescence emission spectra for TiSn0, TiSn3, TiSn5 and TiSn10 measured at room temperature. Excitation wavelength = 300 nm.

the efficiency of charge carrier trapping, immigration, and transfer, and also to understand the recombination rate of electron–hole pairs in semiconductor particles. The emission intensity of the PL spectra has been related closely to the luminescence of the recombination of photoinduced electrons and holes, the free excitons, and self-trapped excitons, which can be affected by crystalline phase, crystalline sizes and surface state. Previous works have reported that the lower the intensity of PL spectra for research samples with similar grain size, the higher photocatalytic activity [54–56]. In our study, the PL emission intensity of Sn^{4+}-doped samples with similar grain size (Table 1) is different, which indicates that TiO_2 incorporating with an appropriate amount of Sn^{4+} may slow the radiative recombination process [57].

The average compositions obtained from ICP-AES (Table 1) in the final $Ti_{1-x}Sn_xO_2$ samples are in very good accordance with those theoretical calculated for their syntheses. This indicates the synthesis of $Ti_{1-x}Sn_xO_2$ nanocrystals from peroxo-metal precursor by the hydrothermal treatment under low temperature is available. In this reaction, the crystal growth occurs during the hydrothermal process, and the nanocrystalline colloidal generated is well dispersed without any disperser. The absolute zeta potentials of all the $Ti_{1-x}Sn_xO_2$ nanocrystal colloids with negative charges are higher than 50.0 mV (Table 1), indicating high stability of the $Ti_{1-x}Sn_xO_2$ nanocrystal colloids. Many hydroxyl groups are absorbed on the surface of $Ti_{1-x}Sn_xO_2$ nanocrystal colloids with mutual repulsion to maintain the high stability.

The growth of $Ti_{1-x}Sn_xO_2$ nanocrystals from peroxo-metal-complex (PMC) precursor in the hydrothermal solution may be expressed by the following equation:

$$2[Ti(OH)_5(OH_2)]^- + H_2O_2 \rightarrow 2[Ti(OH)_3(OOH)_2(OH_2)]^-$$
$$\rightarrow [Ti_2O_5(OH)_4(OH_2)_2]^{2-} \tag{4}$$

$$[Ti_2O_5(OH)_2]^0 + 7H_2O \rightarrow 2[Ti(OH)_4(OH_2)_2]^0 + O_2 \tag{5}$$

$$2[Sn(OH)_5(OH_2)]^- + H_2O_2 \rightarrow 2[Sn(OH)_3(OOH)_2(OH_2)]^-$$
$$\rightarrow [Sn_2O_5(OH)_4(OH_2)_2]^{2-} \tag{6}$$

$$[Sn_2O_5(OH)_2]^0 + 7H_2O \rightarrow 2[Sn(OH)_4(OH_2)_2]^0 + O_2 \tag{7}$$

Fig. 7. Proposed reaction mechanism: (a) undoped anatase TiO_2 samples; (b) low level Sn^{4+}-doped anatase $Ti_{1-x}Sn_xO_2$ samples; (c) high level Sn^{4+}-doped rutile $Ti_{1-x}Sn_xO_2$ samples.

$$(1-x)[Ti(OH)_4(OH_2)_2]^0 + x[Sn(OH)_4(OH_2)_2]^0 \xrightarrow{hydrothermal} Ti_{1-x}Sn_xO_2$$

(8)
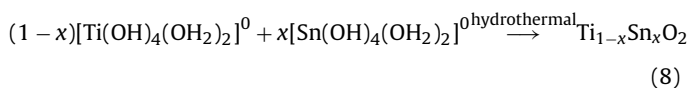
The growth of nanocrystals in the hydrothermal solution occurred via several growth stages in series. In the first growth stage, the PMC formed. In the PMC system, the role of H_2O_2 basically lies with the formation of PMC with metal ions. According to the result of Zhang [58], the peroxo-titanium complex is a dinuclear of two Ti^{4+} ions coordinated by peroxide ligands. This dinuclear peroxo-titanium complex slowly condensed to polynuclear anions. The basic structure in this case is $[(OH)_2TiO_5Ti]^0$ [59]. After heated, the peroxo groups are decomposed and the monomer $[M(OH)_4(OH_2)_2]^0$ (M:Ti or Sn) growing units are formed [60,61]. In the case of the low Sn^{4+} dopant level or undoped condition, $[Ti(OH)_4(OH_2)_2]^0$ is dominant basic unit octahedra. When the basic unit octahedra $[Ti(OH)_4(OH_2)_2]^0$ joined together, sharing other edges leading to anatase has more chances than joining the opposite edge to form rutile (Fig. 7a and b) [62]. At high Sn^{4+} dopant level, the basic unit octahedra $[Sn(OH)_4(OH_2)_2]^0$ increase in the reaction medium. The more $[Sn(OH)_4(OH_2)_2]^0$ exist, the more rutile nuclei can be formed, which results in the $[Ti(OH)_4(OH_2)_2]^0$ units growing epitaxially on it (Fig. 7c) [63]. Thus, the addition of dopant Sn^{4+} affects the crystalline phase structure of the $Ti_{1-x}Sn_xO_2$ samples. This possible growth mechanism can be confirmed with XPS results. From the XPS results, the content of Sn was larger than that of ICP-AES analysis (Table 1). But the deviation (Δ = (surface composition − average composition)/average compostion, ΔTiSn3 = (0.06 − 0.03)/0.03 = 1; ΔTiSn5 = (0.07 − 0.05)/0.05 = 0.4; ΔTiSn10 = (0.14 − 0.1)/0.1 = 0.4) for Sn-doped anatase phase sample TiSn3 is larger than those of sample TiSn5 (two phases anatase and rutile coexist) and sample TiSn10 (rutile phase). The possible explanation is that dopant Sn^{4+} more tends to form a nucleus and induces the formation of rutile, when dopant level is high.

Fig. 8 shows that the photocatalytic degradation corresponds to a pseudo-first-order reaction. Pseudo-first-order kinetics was assumed to calculate the corresponding degradation rate constant
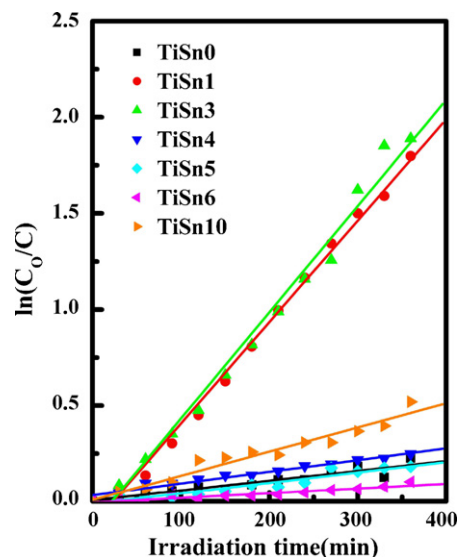
Fig. 8. Linear transform $\ln(C_0/C) = f(t)$ of the kinetic curves of phenol disappearance.

(k):

$$\mathrm{Ln}\left(\frac{C_o}{C}\right) = kt$$

(9)

where C_0 is the original phenol concentration after the adsorption/desorption reached equilibrium ($mg\,L^{-1}$), C is the concentration ($mg\,L^{-1}$) at a given time t (h) and k is the first-order degradation rate constant (h^{-1}). Half-life, $t_{1/2}$ (h), can be calculated from k using the following equation:

$$t_{1/2} = \frac{\mathrm{Ln}\,2}{k}$$

(10)

The photoactivity is calculated and reported as $t_{1/2}$ and degradation rate of phenol in Table 3. The efficiencies of the doped anatase samples (TiSn1 and TiSn3) were almost fourth that of TiSn0, and TiSn3 shows the maximum photoactivity, revealing a positive effect of the presence of tin. Furthermore, the catalyst TiSn4 and TiSn5 with the bicrystalline framework of anatase and rutile show a lower efficiency compared to TiSn1 and TiSn3, which had only the anatase phase. It can be concluded that the tin doping of the anatase phase of TiO_2 is beneficial for the photocatalytic activity in the present study. This interpretation can also be supported by the facts that the decrease of anatase phase proportion from TiSn3 to TiSn6 leads to a lower phenol degradation rate. Generally, the bicrystalline framework of anatase and rutile can effectively reduce the recombination of the photogenerated charge carrier to enhance the photocatalytic activity [64,65]. The low activities of the doped anatase–rutile samples in present study result from the large anatase crystal size,

Table 3
Kinetic values for the phenol photodecomposition and photocatalytic ability results for $Ti_{1-x}Sn_xO_2$ nanocrystal colloids.

Sample	Degradation of phenol (%)[a]	Apparent rate constant k (h^{-1})	Half-life $t_{1/2}$ (h)
TiSn0	21.0	0.0307	22.5
TiSn1	83.4	0.317	2.2
TiSn3	84.9	0.332	2.1
TiSn4	22.9	0.0367	18.9
TiSn5	17.2	0.0327	21.2
TiSn6	9.8	0.0148	46.7
TiSn10	42.6	0.0756	9.2

[a] The samples were irradiation under UV light for 6 h.

which induced poor intimate contact between these two phases and was unable to demonstrate its structure advantages [66]. It should be noted that all the doped samples show higher BET areas than undopant sample (Table 1), which is generally expected to enhanced photocatalytic activity. In the case of the doped rutile samples, TiSn10 shows a better performance than TiSn6, suggesting a positive effect of a higher surface area. However, the photocatalytic activity of the different doped crystalline phase samples such as TiSn3, TiSn5 and TiSn6 varies much, although both the catalysts had similar surface areas. Therefore, the beneficial effect of Sn^{4+} in these samples not only due to higher surface area, but also lies on the crystallization induced by the dopant [47].

On the other hand, the surface state modified by Sn^{4+} incorporation greatly influences the photocatalytic activity. XPS results prove that the percentage of surface oxygen vacancies and surface hydroxyl group is increased by doping Sn^{4+} (Table 2). The surface oxygen vacancies of TiO_2 can induce sub-band levels near the bottom of the conduction band and easily capture photoinduced electrons. It was reported that the photoexcited electron, captured by sub-bands related to oxygen vacancies could enhance the separation of photoexcited chargers, resulting in the improvement of the photocatalytic activity of TiO_2 under UV irradiation [45]. Moreover, surface hydroxyl groups are thought to play an important role in determining photocatalytic activity, since these groups accept holes generated by UV illumination to form hydroxyl radicals and prevent electron–hole recombination. But more oxygen vacancies may act as recombination center and decrease the photocatalytic activity. In our study, the PL emission intensity (peaks with central wavelength beyond 400 nm related to the surface states and oxygen vacancies) of Sn^{4+}-doped samples with similar grain size (Fig. 6) is TiSn3 ≈ TiSn10 < TiSn5. Generally, the lower the intensity of PL spectra for research samples with similar grain size, the higher the photocatalytic activity [54–56]. Our photocatalytic activity (TiSn3 > TiSn10 > TiSn5 > TiSn0) is in agreement with the PL measurement results. From XPS results, the surface oxygen vacancies (SOV) of $Ti_{1-x}Sn_xO_2$ nanocrystal obtained increased in the order of TiSn0 < TiSn3 < TiSn10 < TiSn5. It has to mention that both the surface oxygen vacancies and the surface hydroxyl groups are related to the amounts of Sn^{4+} incorporation in the TiO_2 lattice, and thus, it is understandable that the optimized amount of Sn^{4+} incorporation for TiSn3 endows it with the highest photocatalytic activity.

4. Conclusion

$Ti_{1-x}Sn_xO_2$ nanocrystal colloids have been successfully synthesized from peroxo-metal-complex precursor by hydrothermal method. The obtained compositions are in very good accordance with the calculated value. The major effects of Sn doping are: (i) the formation of Sn-doped anatase phase, two phase (anatase and rutile) coexist and rutile phase with $x < 0.04$, $0.04 < x < 0.06$ and $x \geq 0.06$, respectively, (ii) more smaller rutile crystals than anatase crystals in biphase mixture, (iii) the decrease of the mean crystallite sizes, particle size and surface areas with increased Sn doping, (iv) Sn^{4+} substituted Ti^{4+} into the lattice of TiO_2 alongside increasing the surface oxygen vacancies and the surface hydroxyl groups and (vi) the enhanced light absorption property in the UV region and shifts of absorption edge by Sn^{4+} doping. Regarding to photocatalytic activity for the photocatalytic degradation of phenol, an obvious beneficial effect is observed in Sn-doped TiO_2 samples, was nearly four times higher than undoped samples. The beneficial effect of Sn^{4+} appears to be due to high surface area, optimal crystalline phase and surface state modifications.

References

[1] J. Yuan, S. Zhou, L. Wu, B. You, J. Phys. Chem. B 110 (2006) 388–394.
[2] O. Carp, C.L. Huisman, Solid State Chem. 32 (2004) 33–177.
[3] R.J. James, G. Andrei, M.P. Laurence, S. Patrik, B.W. Alison, Am. Chem. Soc. 130 (2008) 13364–13372.
[4] G.H. Liu, Y.F. Zhu, X.R. Zhang, B.Q. Xu, Anal. Chem. 74 (2002) 6279–6284.
[5] S. Vaidyanathan, Z. Ni, E.G. Seebauer, R.I. Masel, Ind. Eng. Chem. Res. 45 (2006) 3815–3820.
[6] H.G. Yang, G. Liu, S.Z. Qiao, C.H. Sun, Y.G. Jin, S.C. Smith, J. Zou, H.M. Cheng, G.Q. Lu, J. Am. Chem. Soc. 131 (2009) 4078–4083.
[7] P.D. Cozzoli, A. Kornowski, H. Weller, J. Am. Chem. Soc. 125 (2003) 14539–14548.
[8] B. Oregan, M. Gratzel, Nature 373 (1991) 737–740.
[9] K. Yang, J.M. Zhu, J.J. Zhu, S.S. Huang, X.H. Zhu, G.B. Ma, Mater. Lett. 57 (2003) 4639–4642.
[10] S.F. Yang, Y.H. Liu, Y.P. Guo, J.Z. Zhao, H.F. Xu, Z.C. Wang, Mater. Chem. Phys. 77 (2002) 501–506.
[11] M. Wu, G. Lin, D. Chen, G. Wang, D. He, S. Feng, R. Xu, Chem. Mater. 14 (2002) 1974–1980.
[12] X. Bokhimi, A. Morales, O. Novaro, T. López, E. Sánchez, R. Gómez, J. Mater. Res. 10 (1995) 2788–2796.
[13] S. Winardi, R.R. Mukti, K.P. Kumar, J. Wang, Langmuir 26 (2010) 4567–4571.
[14] C.C. Chung, T.W. Chung, T.C. Yang, Ind. Eng. Chem. Res. 47 (2008) 2301–2307.
[15] C.T. Dinh, T.D. Nguyen, F. Kleitz, T.-O. Do, ACS Nano 3 (2009) 3737–3743.
[16] H.K. Yu, G.R. Yi, J.H. Kang, Y.S. Cho, V.N. Manoharan, D.J. Pine, S.M. Yang, Chem. Mater. 20 (2008) 2704–2710.
[17] K.V. Baiju, S. Shukla, K.S. Sandhya, J. James, K.G.K. Warrier, J. Phys. Chem. C 111 (2007) 7612–7622.
[18] A. Zachariah, K.V. Baiju, S. Shukla, K.S. Deepa, J. James, K.G.K. Warrier, J. Phys. Chem. C 112 (2008) 11345–11356.
[19] H.Z. Zhang, J.F. Banfield, J. Phys. Chem. B 104 (2000) 3481–3487.
[20] X. Bokhimi, A. Morales, F. Pedraza, J. Solid State Chem. 169 (2002) 176–181.
[21] S. Yin, H. Hasegawa, D. Maed, M. Ishitsuka, T. Sato, J. Photochem. Photobiol. A 163 (2004) 1–8.
[22] Y. Li, J. Liu, Z. Jia, Mater. Lett. 60 (2006) 1753–1757.
[23] C. Suresh, V. Biju, P. Mukundan, K.G.K. Warrier, Polyhedron 17 (1998) 3131–3135.
[24] M. Gopal, W.J. Mobey Chan, L.C. De Jonghe, J. Mater. Sci. 32 (1997) 6001–6008.
[25] H. Uchiyama, H. Imai, Chem. Commun. 48 (2005) 6014–6016.
[26] C. Xiong, X. Deng, J. Li, Appl. Catal. B 94 (2010) 234–240.
[27] G. Sankar, K.R. Kajman, C.N.R. Rao, Catal. Lett. 8 (1991) 27–36.
[28] Y. Li, Y. Fan, H. Yang, B. Xu, L. Feng, M. Yang, Y. Chen, Chem. Phys. Lett. 372 (2003) 160–165.
[29] J.H. Liao, L.Y. Shi, S. Yuan, Y. Zhao, J. Phys. Chem. C 113 (2009) 18778–18783.
[30] H.M. Luo, C. Wang, Y.S. Yan, Chem. Mater. 15 (2003) 3841–3846.
[31] F.R. Sensato, R. Custodio, E. Longo, A. Beltrán, J. Andrés, Catal. Today 85 (2003) 145–152.
[32] Y.Q. Cao, T. He, L.S. Zhao, E.J. Wang, W.S. Yang, Y.A. Cao, J. Phys. Chem. C 113 (2009) 18121–18124.
[33] J. Ovenstone, P.J. Titler, R. Withnall, J. Silver, J. Phys. Chem. B 105 (2001) 7170–7177.
[34] T. Hirata, K. Ishioka, M. Kitajima, H. Doi, Phys. Rev. B 53 (1996) 8442–8448.
[35] F. Fresno, D. Tudela, J.M. Coronado, J. Soria, Catal. Today 143 (2009) 230–236.
[36] E. Chinarro, B. Moreno, J.R. Jurado, J. Eur. Ceram. Soc. 27 (2007) 3601–3604.
[37] E.M. El-Maghraby Nakamura, S. Rengakuji, Catal. Commun. 9 (2008) 2357–2360.
[38] F. Fresno, D. Tudela, M. Juan, Phys. Chem. Chem. Phys. 8 (2006) 2421–2430.
[39] F. Sayılkana, M. Asiltürka, N. Kirazb, J. Hazard. Mater. 162 (2009) 1309–1316.
[40] J. Overstone, K. Yanagisawa, Chem. Mater. 11 (1999) 2770–2774.
[41] R.Y. Zheng, L. Lin, J.L. Xie, Y.X. Zhu, Y.C. Xie, J. Phys. Chem. C 112 (2008) 15502–15509.
[42] M.M. Oliveira, D.C. Schnitzler, A.J.G. Zarbin, Chem. Mater. 15 (2003) 1903–1909.
[43] L.C. Chena, F.R. Tsai, S.H. Fang, Y.C. Ho, Electrochim. Acta 54 (2009) 1304–1311.
[44] A. Leonardy, W.Z. Hung, D.S. Tsai, C.C. Chou, Y.S. Huang, Cryst. Growth Des. 9 (2009) 3958–3963.
[45] Y. Zhao, C.Z. Li, X.L. Liu, F. Gu, H.L. Du, L.Y. Shi, Appl. Catal. B 79 (2008) 208–215.
[46] R. Sanjines, H. Tang, H. Berger, F. Gozzo, G. Margaritondo, J. Appl. Phys. 75 (1994) 1952–2945.
[47] Y. Cao, W. Yang, W. Zhang, G. Liu, P. Yue, New J. Chem. 28 (2004) 218–222.
[48] J.G. Yu, H.G. Yu, B. Cheng, X.J. Zhao, J.C. Yu, W.K. Ho, J. Phys. Chem. B 107 (2003) 13871–13879.
[49] B. Xin, L. Jin, Z. Ren, B. Wang, H. Fu, J. Phys. Chem. B 109 (2005) 2805–2809.
[50] Y. Wang, N. Herron, J. Phys. Chem. 95 (1991) 525–532.

[51] M.H. Zhou, J.G. Yu, S.W. Liu, P. Zhai, L. Jiang, J. Hazard. Mater. 154 (2008) 1141–1148.
[52] M.A. Khan, O.B. Yang, Cryst. Growth Des. 9 (2009) 1767–1774.
[53] N. Serpone, D. Lawless, R. Khairutdinov, J. Phys. Chem. 99 (1995) 16646–16654.
[54] Y. Cong, J.L. Zhang, F. Chen, M. Anpo, D.N. He, J. Phys. Chem. C 111 (2007) 10618–10623.
[55] J.C. Yu, J.G. Yu, W.K. Ho, Z. Jiang, L.Z. Zhang, Chem. Mater. 14 (2002) 3808–3816.
[56] Y. Cong, J.L. Zhang, F. Chen, M. Anpo, J. Phys. Chem. C 111 (2007) 6976–6982.
[57] M.A. Khan, H.T. Jung, O.B. Yang, J. Phys. Chem. B 110 (2006) 6626–6630.
[58] Y. Zhang, L.Z. Wu, Q.H. Zeng, J.F. Zhi, J. Phys. Chem. C 112 (2008) 16457–16462.
[59] C. Ribeiro, C. Vila, D.B. Stroppa, V.R. Mastelaro, J. Bettini, E. Longo, E.R. Leite, J. Phys. Chem. C 111 (2007) 5871–5875.
[60] J. Muhlebach, K. Muller, G. Schwarzenbach, Inorg. Chem. 9 (1970) 2381–2390.
[61] H. Ichinose, M. Terasaki, H. Katsuki, J. Sol–Gel Sci. Technol. 22 (2001) 33–40.
[62] B.Z. Tian, F. Chen, J.L. Zhang, M. Anpo, J. Colloid Interface Sci. 303 (2006) 142–148.
[63] K.P. Kumar, D.J. Fray, J. Nair, F. Mizukamic, T. Okubo, Scripta Mater. 57 (2007) 771–774.
[64] D.C. Hurum, A.G. Agrios, K.A. Gray, J. Phys. Chem. B 107 (2003) 4545–4549.
[65] L. Shi, D. Weng, J. Environ. Sci. 20 (2008) 1263–1267.
[66] X.T. Hong, Z.P. Wang, W.M. Cai, Chem. Mater. 17 (2005) 1548–1552.